Supporting Information for Charge Carrier Dynamics in Two-Dimensional Hybrid Perovskites: Dion-Jacobson vs. Ruddlesden-Popper Phases

Dibyajyoti Ghosh,[*,†,‡] Debdipto Acharya,[¶,§] Laurent Pedesseau,[‖] Claudine Katan,[⊥] Jacky Even,[‖] Sergei Tretiak,[†,‡,#] and Amanda J. Neukirch[*,†]

†*Theoretical Division, Los Alamos National Laboratory, Los Alamos, NM, 87545, USA*

‡*Center for Nonlinear Studies, Los Alamos National Laboratory, Los Alamos, NM, 87545, USA*

¶*Theoretical Sciences Unit, Jawaharlal Nehru Centre for Advanced Scientific Research, Bangalore, 560064, India*

§*Present Address: Univ Rennes, INSA Rennes, CNRS, Institut FOTON - UMR 6082, F-35000 Rennes, France*

‖*Univ Rennes, INSA Rennes, CNRS, Institut FOTON - UMR 6082, F-35000 Rennes, France*

⊥*Univ Rennes, ENSCR, INSA Rennes, CNRS, ISCR - UMR 6226, F-35000 Rennes, France*

#*Center for Integrated Nanotechnologies, Los Alamos National Laboratory, Los Alamos, NM, 87545, USA*

E-mail: dibyajyoti@lanl.gov; ajneukirch@lanl.gov

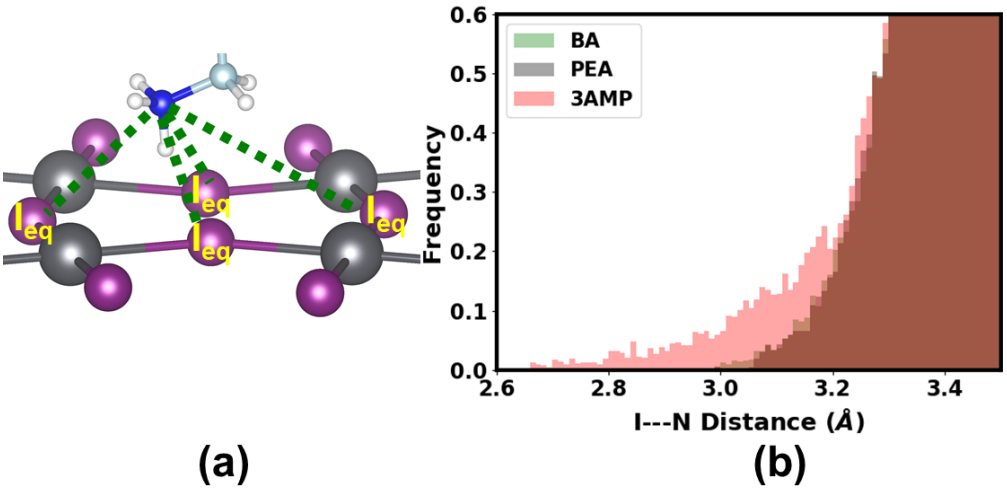

Figure S 1: The dynamic interactions between spacer cations and inorganic framework. (a) Schematic of distances among N of NH_3 group of the spacer cation and equatorial iodine atoms of the inorganic slab. (b) Histograms of N—I distances for 2D-perovskites. The distance distribution histograms shows short N...I instantaneous distances ($<$ 3 Å) in the DJ-phase perovskite.

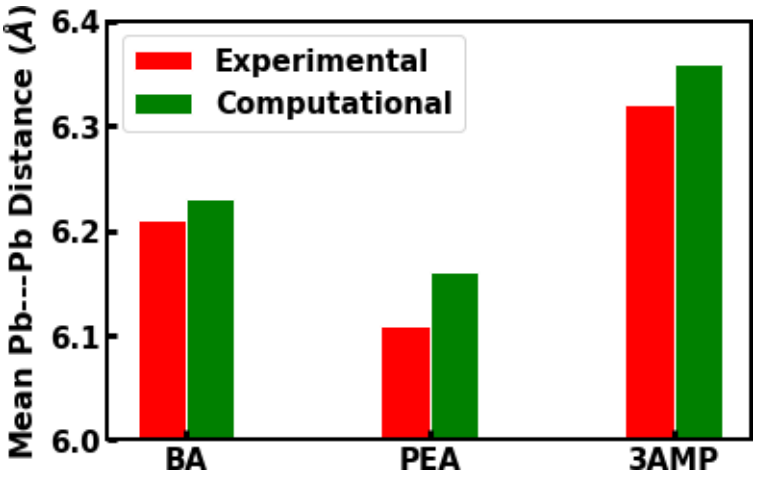

Figure S 2: Comparison between experimentally reported and computationally calculated Pb...Pb distances. The experimental values are extracted from reported X-ray diffraction data of $(BA)_2PbI_4$,[1] $(PEA)_2PbI_4$,[2] and $(3\,AMP)PbI_4$[3]. We calculate the time averaged distances between nearest Pb atoms of the inorganic framework for these 2D perovskites from AIMD trajectories. Experimental and computational Pb...Pb distances are consistent for all three 2D perovskites. The expansion of lead iodide framework due to bulky 3AMP spacer cations is evident from longer averaged Pb...Pb distance for $(3\,AMP)PbI_4$.

S1. Dynamic Pb-I distances

Due to the dimensionality of the perovskite framework, there are two geometrically distinct Pb-I bonds, that are, axial and equatorial bonds (Fig. S3a) in 2D-perovskites. In Fig. S3b-c, plotted histogram of both types of Pb-I bond lengths exhibit similar mode values 3.17-3.20 Å for all three 2D-perovskites. Overall Pb-I distribution is marginally broad for DJ-phase perovskite compared to RP-phase ones. We also find that the axial Pb-I bonds are more broadly distributed compared to the equatorial bonds for all three 2D-perovskites (see Fig. S3d for representative $(3\,\mathrm{AMP})\mathrm{PbI}_4$). Due to the bonding with only one Pb, axial iodine atoms are free to thermally fluctuate compared to equatorial iodine sites that are bonded to two Pb atoms. Different chemical bonding consequently results in slightly dissimilar thermal fluctuations in axial and equatorial Pb-I bond lengths. The Pb-I distributions in Fig. S3b-d are non-Gaussian in nature, clearly demonstrating the significant anharmonic character of lead-iodide based inorganic frames in these 2D-perovskites. Similar anharmonicity of metal halide bonds in 3D-perovskites has been widely discussed.[4–7] Our unconstrained AIMD generated structural trajectories successfully capture this vital character of the Pb-I frames, which dominantly controls the charge carrier dynamics in these halide perovskites.[8] To conclude, the overall distribution of Pb-I bonds are very similar for RP- and DJ-phase 2D-perovskites.

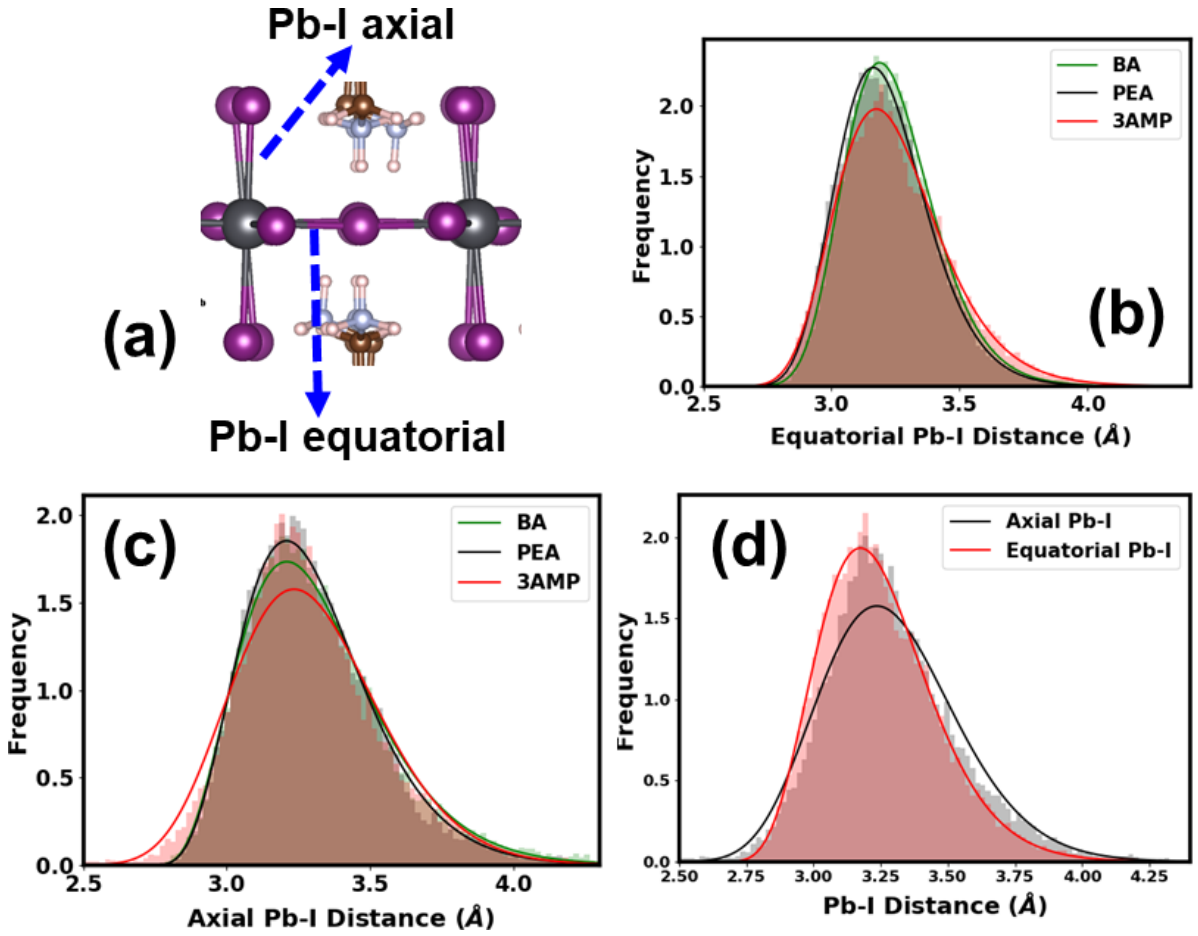

Figure S 3: Pb-I bond length distributions in 2D-perovskites. (a) Schematic of the equatorial and axial Pb-I bonds in 2D-perovskites. Distribution of (b) equatorial and (c) axial Pb-I bond lengths over time for $(BA)_2PbI_4$, $(PEA)_2PbI_4$, and $(3\,AMP)PbI_4$. (d) The distribution of axial and equatorial Pb-I bonds in $(3\,AMP)PbI_4$. We consider the DJ-phase perovskite as the representative system. Note that, RP-phase perovskites also exhibit similar Pb-I distribution characteristics. Solid lines in (b-d) are fitted by beta-function to the distributions.

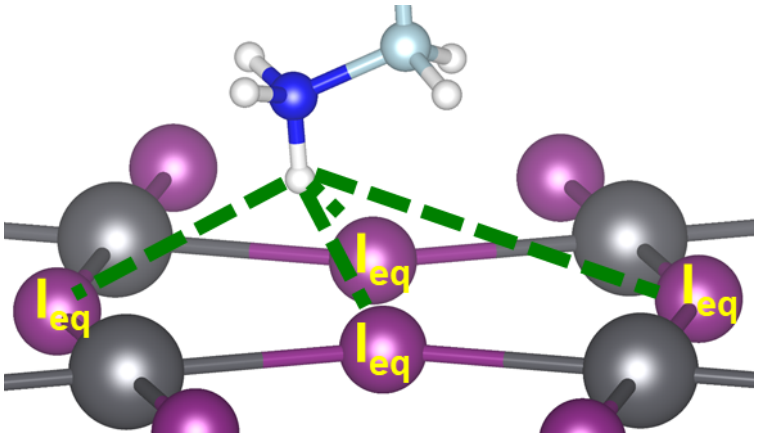

Figure S 4: Schematic of distances among H atoms of NH_3 group of the spacer cation and equatorial iodine atoms of the inorganic slab.

S2. Effect of Non-covalent Interactions on Equatorial Iodide Site

The hydrogen-bond formation between H of NH_3 groups and equatorial iodide sites can affect the thermal motions of the acceptor sites. Note that, the spacer cation induces in-plane expansion of the PbI-slab, leading one to expect higher thermal fluctuations of equatorial iodide sites in 3AMP-based perovskites. However, hydrogen bonding formation can partially suppress their dynamical activities. To quantitatively verify, we calculate the root-mean square fluctuations (RMSF) of the equatorial iodide sites for $(3\,\mathrm{AMP})PbI_4$ and $(BA)_2PbI_4$. The higher the RMSF of a lattice-site, the more spatial fluctuations are expected for this site. The evaluated RMSF for $(3\,\mathrm{AMP})PbI_4$ and $(BA)_2PbI_4$ are 0.55 Å and 0.88 Å, respectively. The smaller RMSF unambiguously depicts the reduced motion of the equatorial iodine atoms in the DJ-phase perovskite, originating from the stronger non-covalent H...I interactions. Thus, higher intrusion depth of NH_3 and consequent formation of stronger non-covalent H...I interactions partially suppress the thermal motions of equatorial iodides in $(3\,\mathrm{AMP})PbI_4$.

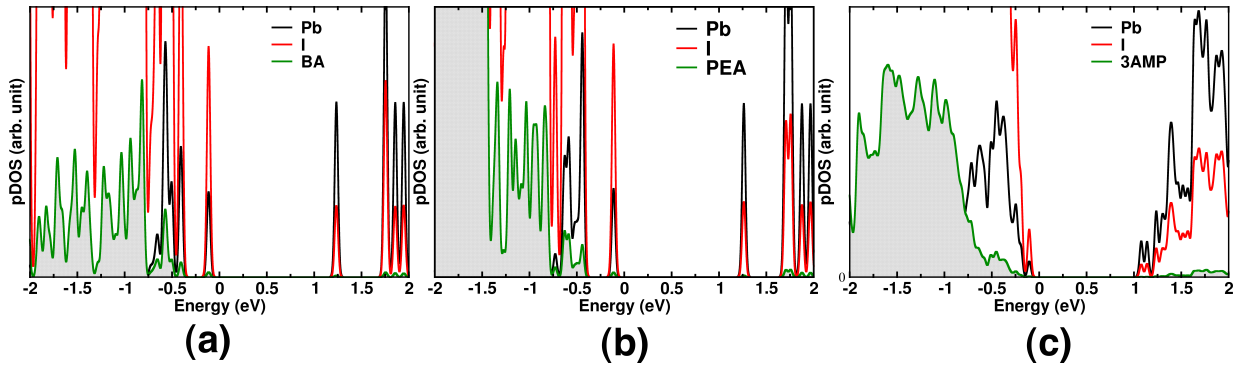

Figure S 5: Electronic structures of 2D-perovskites. Partial density of states for (a)$(BA)_2PbI_4$, (b) $(PEA)_2PbI_4$, and (c) $(3\,\mathrm{AMP})PbI_4$. The electronic structures are calculated using PBE-GGA+SOC level of theory.

Table S 1: The standard deviation (stdv) of band edge state fluctuations along AIMD trajectories of 2D-perovskites. The values are calculated from PBE based simulations.

Perovskites	Standard deviation in VBM (eV)	Standard deviation in CBM (eV)
$(BA)_2PbI_4$	0.10	0.08
$(PEA)_2PbI_4$	0.90	0.11
$(3\,\mathrm{AMP})PbI_4$	0.90	0.07

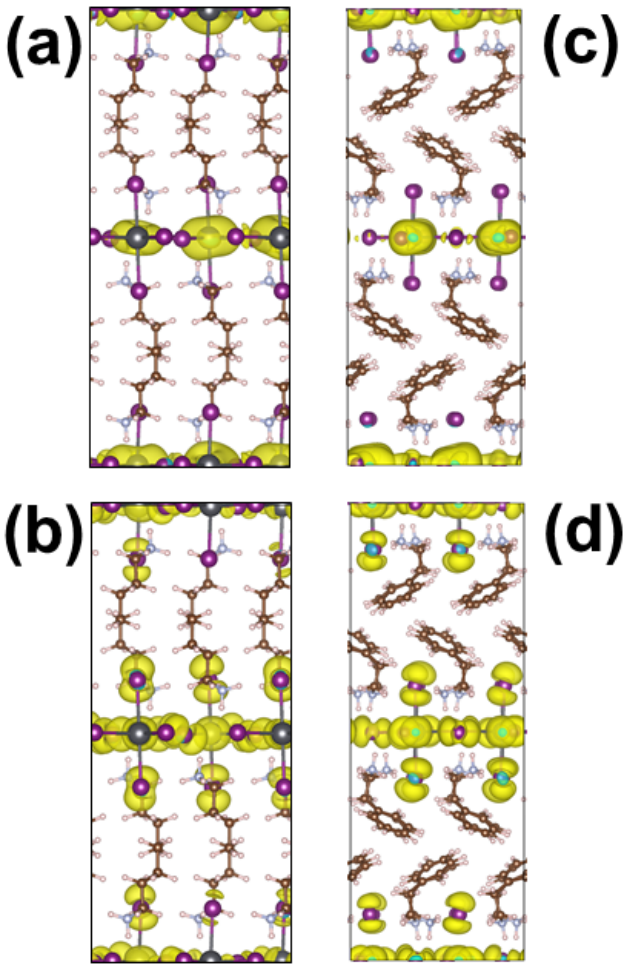

Figure S 6: The electronic charge densities of (a) CBM and (b) VBM for $(BA)_2PbI_4$. And (c) CBM and (d) VBM charge densities for $(PEA)_2PbI_4$. The band edges are delocalized over the PbI-framework. The electronic structures are calculated using PBE+SOC level of theory.

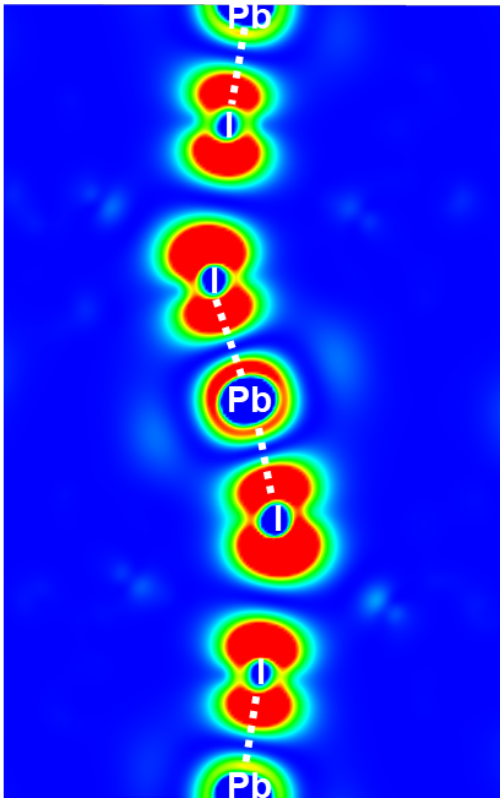

Figure S 7: Electronic charge density of the VBM for $(BA)_2PbI_4$. Color code: blue and red depict 0 and 0.000125 eÅ^{-3}. The white dotted lines indicate the Pb-I covalent bonds. The electronic structures are calculated using PBE-GGA+SOC level of theory.

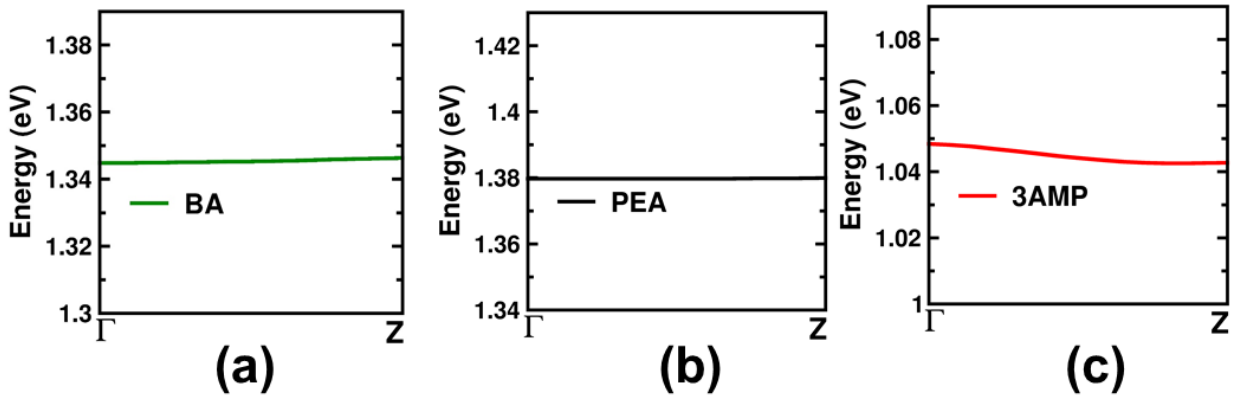

Figure S 8: Comparison of conduction band dispersion curves along the stacking axis for (a) $(BA)_2PbI_4$, (b) $(PEA)_2PbI_4$, and (c) $(3\,AMP)PbI_4$. Almost flat band dispersion suggests weak interaction of CBM band along the stacking direction.

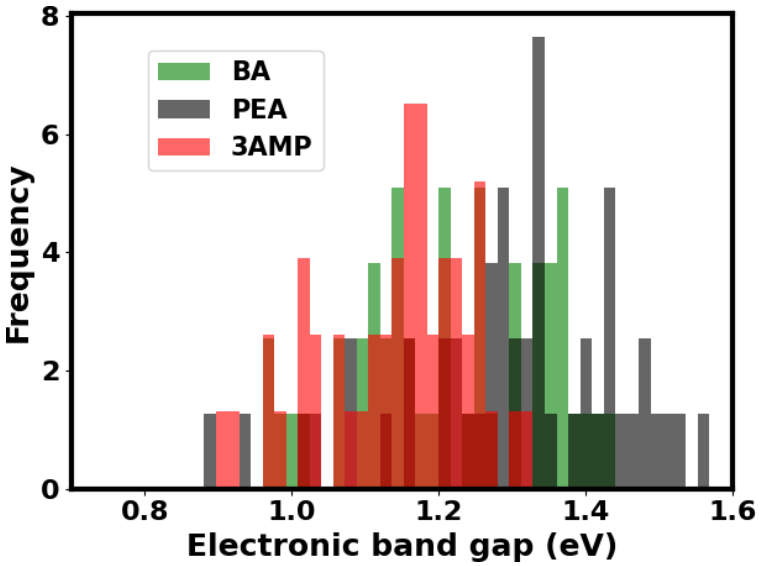

Figure S 9: The histogram distribution of PBE-GGA+SOC electronic band gaps along the AIMD trajectories for 2D-perovskites. We have considered 100 snapshots of structures that are equally spaced in time to calculate the electronic band gap distributions.

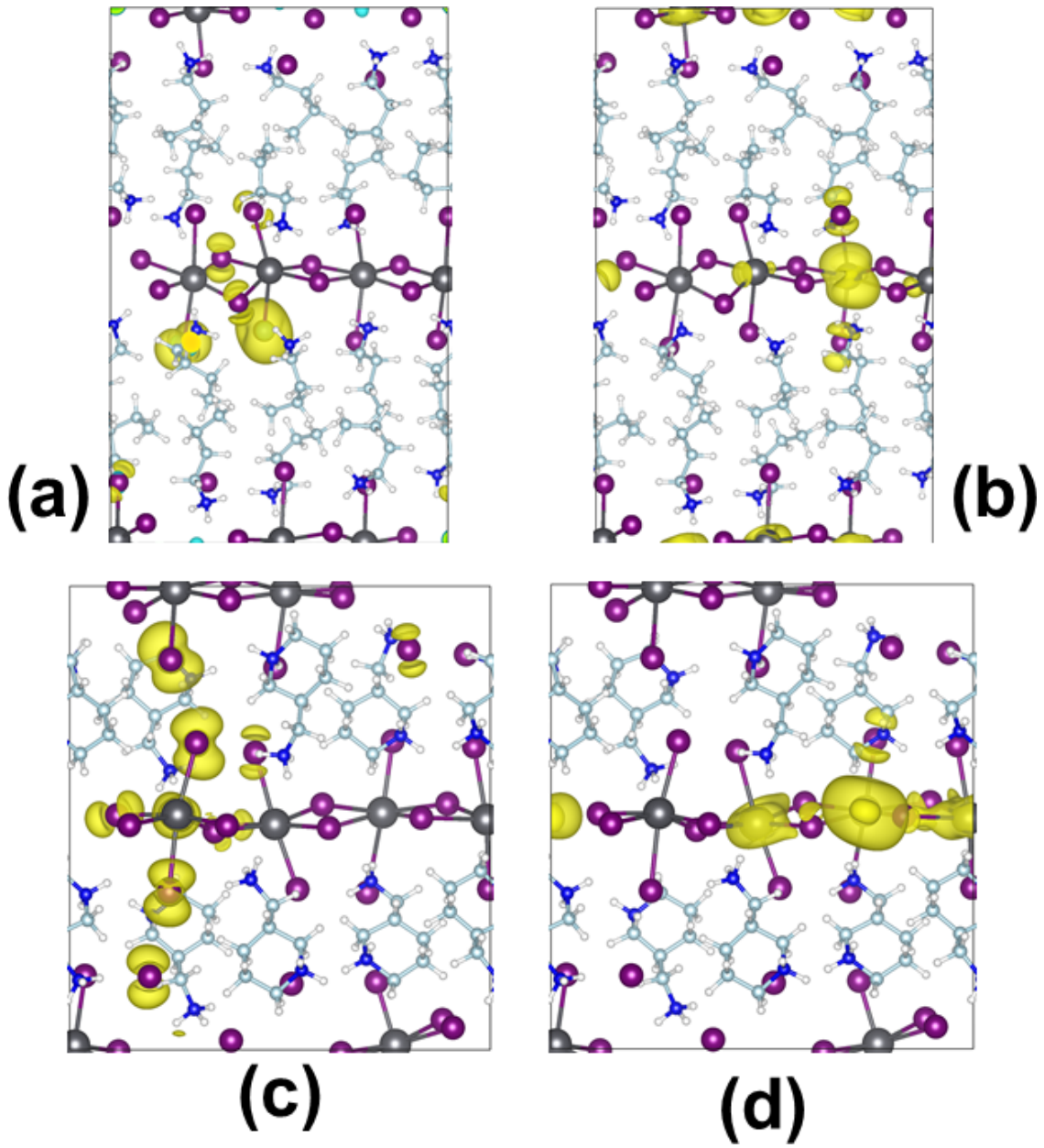

Figure S 10: Effect of the SOC in instant band edge charge densities. The instant (a) VBM and (b) CBM charge densities for the time steps with highest NAC (i.e. 0.0084 eV) in $(BA)_2PbI_4$. The instant (c) VBM and (d) CBM charge densities of $(3\,AMP)PbI_4$ at the snapshot of time with the highest NAC (0.0056 eV). The band edge charge densities remain mostly unchanged with incorporation of SOC corrections in the charge density calculation.

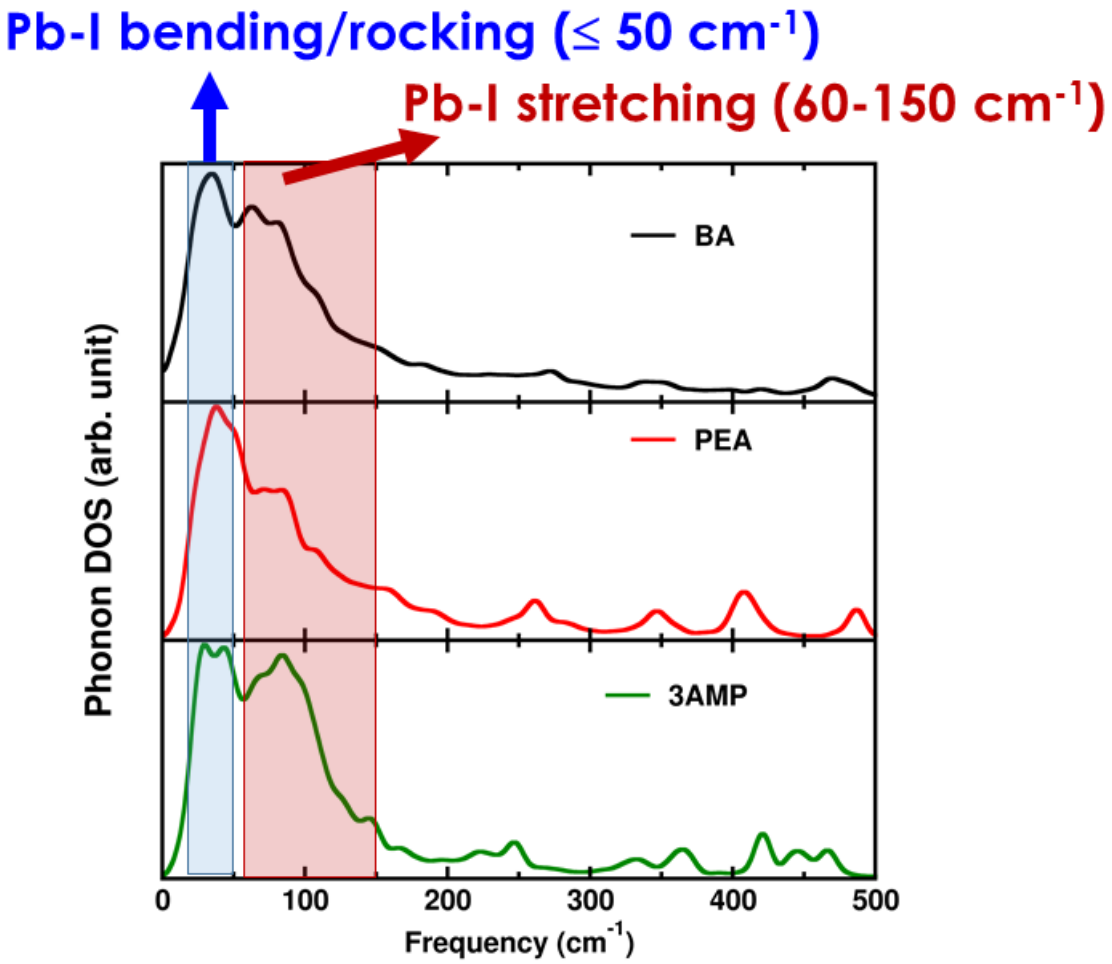

Figure S 11: Low-frequency vibrational modes of 2D perovskites. The total vibrational density of states (vDOS) of $(BA)_2PbI_4$ (upper panel), $(PEA)_2PbI_4$ (middle panel), and $(3\,AMP)PbI_4$ (lower panel). As assigned by Balaji *et al.*,[9] the peaks ≤ 50 cm^{-1} arise from Pb-I bending and rocking modes. In the frequency range of 60-150 cm^{-1}, the Pb-I stretching modes appear. We calculate the vDOS by performing Fourier transformation of the mass-weighted velocity auto-correlation function obtained from AIMD simulations. TRAVIS program package has been used to calculate vDOS.[10]

S3. Influence Spectra for 2D-perovskites

To reveal the virbational modes of the system that participate in the energy dissipation during the non-adiabatic transitions we compute the phonon influence spectra. They are obtained by performing performing Fourier transformation of the band gap autocorrelation function. Details of the computational formulation can be found elsewhere.[11–13] The peaks in the spectra reveal the vibrational modes of the system that participate in the energy dissipation during the non-adiabatic transition.

The low-frequency peaks at the range of 0 - 150 cm^{-1} dominantly appear from Pb-I framework as we discuss in the main text.[9] Here, we evaluate the origin of the peaks that are at higher frequency range 150-400 cm^{-1} and appear from the molecular vibrations coupled to the lattice dynamics of the inorganic layer. We calculate the vibrational spectra for gas-phase spacer molecules to understand the modes that actively contribute to the non-radiative energy losses in 2D-perovskites. As shown in Fig. S12a, for BA in $(BA)_2PbI_4$, the rocking mode of $-NH_3$ group contributes the intense peak at 243 cm^{-1}. We assign the peak at 342 cm^{-1} which is common for all three spacer cations to the scissoring (bending) mode of cation framework (Fig. S12b). For PEA, we assign rocking modes of $-CH_2NH_3$ group to the peak at 263 cm^{-1} (Fig. S12c). The peak at 342 cm^{-1} for PEA appears from complex bending modes of $-CH_2CH_2NH_3$ group. For (3 AMP)PbI_4, the intense 201 cm^{-1} peak assigns to the rocking mode of $-NH_3$ group of 3AMP molecule (Fig. S12e). Whereas, the scissoring (bending) mode of 3AMP produces the peak at 342 cm^{-1} (Fig. S12f).

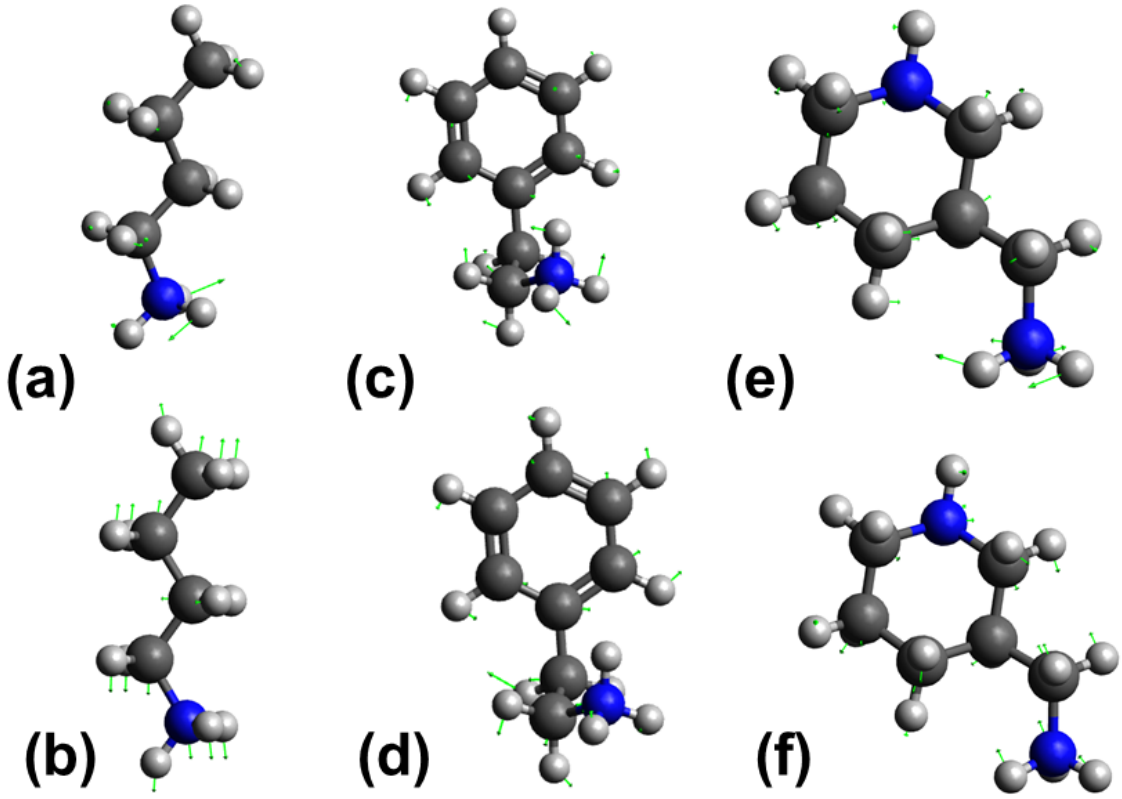

Figure S 12: Low-frequency molecular vibrational modes of spacer cations. Vibrational modes of BA cation at (a) 243 cm^{-1} and (b) 342 cm^{-1}. The modes of PEA cations at (c) 263 cm^{-1} and (d) 342 cm^{-1}. The modes of 3AMP at (e) 200 cm^{-1} and (f) 342 cm^{-1}. Green arrows represent the direction of atomic displacements in a particular vibrational mode.

S4. Elastic electron-phonon interactions

We calculate the pure-dephasing functions using the second-order cumulant approximation of the optical response theory to understand the elastic electron-phonon interactions.[14–16] In Fig. S13, the plotted pure-dephasing functions show marginally faster decoherence of VBM-CBM states for $(BA)_2PbI_4$ and $(PEA)_2PbI_4$ compared to that for $(3\,AMP)PbI_4$. We calculate the dephasing time (τ) for each system by fitting the obtained function to a single-Gaussian function having the form of $f(t) = \exp(-(t/\tau)^2/2)$.[17] The dephasing times as listed in Table 1 of main text, are very similar for all three 2D-perovskites. Slightly faster dephasing in RP-phase perovskites originate from their higher extent of thermal fluctuations compared to DJ-phase perovskite.

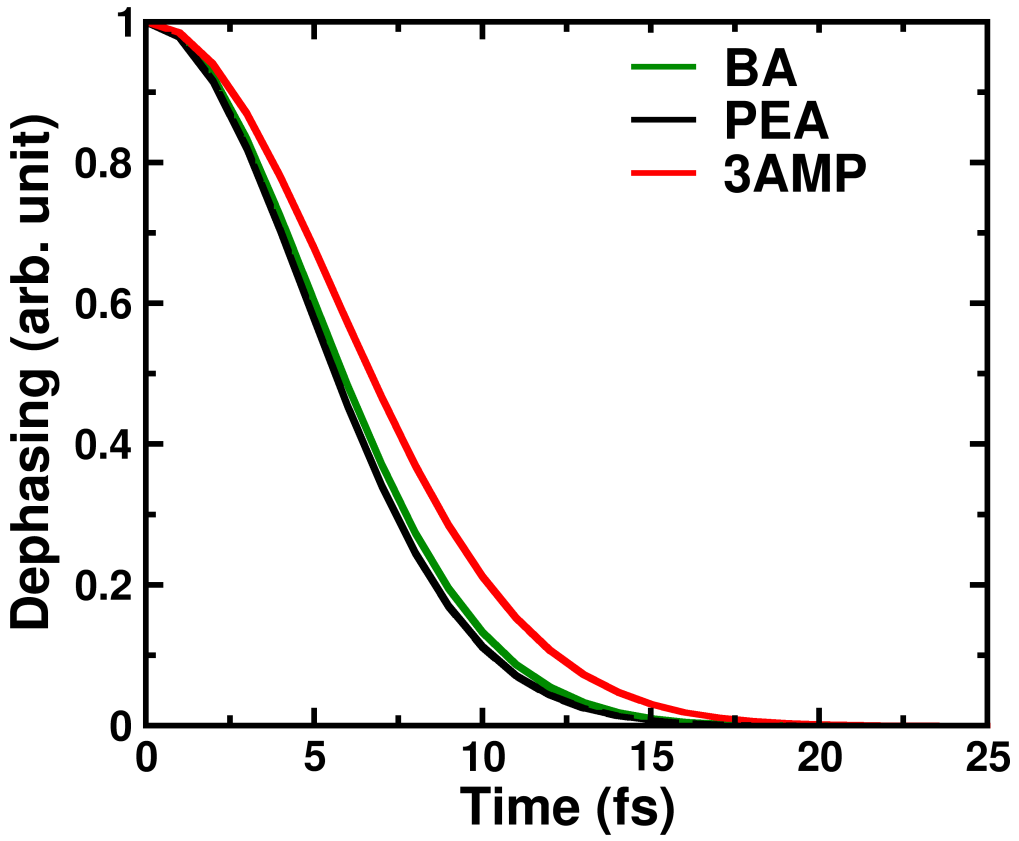

Figure S 13: Influence of spacer cations in elastic electron-phonon interactions in 2D-perovskites. The decay time of pure-dephasing functions for the VBM-CBM transition in $(BA)_2PbI_4$, $(PEA)_2PbI_4$, and $(3\,AMP)PbI_4$.

S5. Calculating the electron-hole recombination time

We employ short-time linear approximation to model the exponential increase of the recombined charge population in the ground state of the 2D perovskites. This further evaluates the electron-hole nonradiative recombination time across the electronic band gap (see Fig. 5a, main manuscript). The non-radiative recombination time (τ) can be simulated by fitting the population increase to the following equation,

$g(t) = 1 - \exp(-t/\tau)$

Similar function has been applied already to calculate the carrier recombination time in halide perovskites.[18]

References

(1) Billing, D. G.; Lemmerer, A. Synthesis, characterization and phase transitions in the inorganic–organic layered perovskite-type hybrids [(CnH2n+ 1NH3) 2PbI4], n= 4, 5 and 6. *Acta Crystallographica Section B: Structural Science* **2007**, *63*, 735–747.

(2) Yang, S.; Niu, W.; Wang, A.-L.; Fan, Z.; Chen, B.; Tan, C.; Lu, Q.; Zhang, H. Ultrathin two-dimensional organic–inorganic hybrid perovskite nanosheets with bright, tunable photoluminescence and high stability. *Angewandte Chemie International Edition* **2017**, *56*, 4252–4255.

(3) Mao, L.; Ke, W.; Pedesseau, L.; Wu, Y.; Katan, C.; Even, J.; Wasielewski, M. R.; Stoumpos, C. C.; Kanatzidis, M. G. Hybrid Dion–Jacobson 2D lead iodide perovskites. *J. Am. Chem. Soc* **2018**, *140*, 3775–3783.

(4) Mayers, M. Z.; Tan, L. Z.; Egger, D. A.; Rappe, A. M.; Reichman, D. R. How lattice and charge fluctuations control carrier dynamics in halide perovskites. *Nano Lett.* **2018**, *18*, 8041–8046.

(5) Munson, K. T.; Swartzfager, J. R.; Asbury, J. B. Lattice Anharmonicity: A Double-

Edged Sword for 3D Perovskite-Based Optoelectronics. *ACS Energy Lett.* **2019**, *4*, 1888–1897.

(6) Katan, C.; Mohite, A. D.; Even, J. Entropy in halide perovskites. *Nature materials* **2018**, *17*, 377–379.

(7) Carignano, M. A.; Aravindh, S. A.; Roqan, I. S.; Even, J.; Katan, C. Critical fluctuations and anharmonicity in lead iodide perovskites from molecular dynamics supercell simulations. *The Journal of Physical Chemistry C* **2017**, *121*, 20729–20738.

(8) Whalley, L. D.; Skelton, J. M.; Frost, J. M.; Walsh, A. Phonon anharmonicity, lifetimes, and thermal transport in CH 3 NH 3 PbI 3 from many-body perturbation theory. *Physical Review B* **2016**, *94*, 220301.

(9) Dhanabalan, B.; Leng, Y.-C.; Biffi, G.; Lin, M.-L.; Tan, P.-H.; Infante, I.; Manna, L.; Arciniegas, M. P.; Krahne, R. Directional Anisotropy of the Vibrational Modes in 2D-Layered Perovskites. *ACS nano* **2020**, *14*, 4689–4697.

(10) Brehm, M.; Kirchner, B. TRAVIS-a free analyzer and visualizer for Monte Carlo and molecular dynamics trajectories. 2011.

(11) Akimov, A. V.; Prezhdo, O. V. The PYXAID program for non-adiabatic molecular dynamics in condensed matter systems. *Journal of chemical theory and computation* **2013**, *9*, 4959–4972.

(12) Akimov, A. V.; Prezhdo, O. V. Advanced capabilities of the PYXAID program: integration schemes, decoherence effects, multiexcitonic states, and field-matter interaction. *Journal of chemical theory and computation* **2014**, *10*, 789–804.

(13) Jankowska, J.; Long, R.; Prezhdo, O. V. Quantum dynamics of photogenerated charge carriers in hybrid perovskites: Dopants, grain boundaries, electric order, and other realistic aspects. *ACS Energy Lett.* **2017**, *2*, 1588–1597.

(14) Hamm, P. Principles of nonlinear optical spectroscopy: A practical approach. *University of Zurich* **2005**, *41*, 77.

(15) Liu, J.; Kilina, S. V.; Tretiak, S.; Prezhdo, O. V. Ligands slow down pure-dephasing in semiconductor quantum dots. *ACS Nano* **2015**, *9*, 9106–9116.

(16) Neukirch, A. J.; Hyeon-Deuk, K.; Prezhdo, O. V. Time-domain ab initio modeling of excitation dynamics in quantum dots. *Coord. Chem. Rev.* **2014**, *263*, 161–181.

(17) Zhang, Z.; Fang, W.-H.; Long, R.; Prezhdo, O. V. Exciton Dissociation and Suppressed Charge Recombination at 2D Perovskite Edges: Key Roles of Unsaturated Halide Bonds and Thermal Disorder. *J. Am. Chem. Soc* **2019**, *141*, 15557–15566.

(18) Nijamudheen, A.; Akimov, A. V. Criticality of symmetry in rational design of chalcogenide perovskites. *J. Phys. Chem. Lett.* **2017**, *9*, 248–257.